Check for updates

Tuning analog resistive switching and plasticity in bilayer transition metal oxide based memristive synapses†

Jingxian Li,[ab] Qingxi Duan,[a] Teng Zhang,[a] Minghui Yin,[a] Xinhao Sun,[a] Yimao Cai,[ac] Lidong Li, [ID] *[b] Yuchao Yang [ID] *[ac] and Ru Huang*[ac]

Memristive devices with analog resistive switching characteristics are widely investigated nowadays for electronic synapses that facilitate memory and learning in neuromorphic computing hardware. It is therefore essential to understand and optimize the incremental switching behavior of the cells in order to enhance the functionality of memristive neural networks. Here we report a systematic study on the analog switching of bilayer oxide based memristive synapses and show that transition metal oxides with rich intermediate phases, such as WO_x, are able to provide larger number of conductance states compared with oxides with few intermediate phases such as TaO_x and HfO_x. This could be attributed to the intrinsically different electrical properties of the intermediate phases that jointly contribute to the change of device conductance, in addition to that caused by the varied geometry of filaments during programming. Controlled studies adopting different materials, compositions and sequences of oxide bilayers reveal that the analog switching is mainly dominated by the switching layer, thus providing clues to the optimization of memristive devices for future neuromorphic applications.

1. Introduction

Memristors, theoretically proposed in 1971,[1] are 2-terminal nanoionic devices that could potentially serve as building blocks for future memory and computing applications due to their high scalability, low power consumption, and excellent compatibility with complementary metal oxide semiconductor (CMOS) technology.[1-8] In 2008, HP Labs linked the concept of memristors with experimentally found resistive switching (RS) devices,[2] and since then their application in non-von Neumann computing paradigms especially neuromorphic computing has been widely exploited.[9] In the envisioned neuromorphic systems, memristors are usually utilized to implement the functionality of synapses in a compact way and therefore enable learning and memory in resultant neural networks. The synaptic plasticity that can be achieved at the device level fundamentally determines the functionality of the constructed networks. A number of synaptic functions have been emulated using memristors till now, such as spike timing dependent plasticity,[10] paired pulse facilitation,[11] heterosynaptic plasticity,[12,13] etc.

It should be noted that the requirement placed on device characteristics in neuromorphic computing significantly departs from that in nonvolatile memory application, e.g. in terms of the number of states (NOS) that can be reliably accessed during resistive switching. To date, synaptic devices based on various binary transition metal oxides such as TaO_x,[14,15] HfO_x,[16-18] TiO_x[19-22] and WO_x[23-28] have been widely studied. The RS behaviors have been further engineered by introducing different interfacial layers and forming a bilayer structure.[29-39] However, it is still unclear how the switching materials should be optimized in order to better fit the requirement in synaptic applications.

In this work, we have systematically studied the analog switching characteristics in memristive synapses based on bilayer oxide structures composed of a switching layer and a base layer. Through controlled investigations on the materials, compositions and stacking sequences of the oxide bilayer, it was found that the switching layer plays a dominant role in the analog switching. More importantly, the existence of rich suboxide phases in the switching layer material was found to be favorable for increasing the number of weight states, despite the fact that the intermediate oxide phases are usually deemed undesirable for nonvolatile memory applications. The richness of multilevel states could be attributed to the different electrical properties of the suboxide phases that jointly contributes to the

[a]Key Laboratory of Microelectronic Devices and Circuits (MOE), Institute of Microelectronics, Peking University, Beijing 100871, China. E-mail: yuchaoyang@pku.edu.cn; ruhuang@pku.edu.cn

[b]State Key Lab for Advanced Metals and Materials, School of Materials Science and Engineering, University of Science and Technology Beijing, Beijing 100083, China. E-mail: lidong@mater.ustb.edu.cn

[c]Innovation Center for MicroNanoelectronics and Integrated System, Beijing 100871, China

† Electronic supplementary information (ESI) available. See DOI: 10.1039/c7ra07522g

change of device conductance, in addition to that caused by the varied geometry of filaments during programming. The findings in this work could shed light on the mechanism of analog switching in oxide memristors and provide clues to further optimization of memristive synapses.

2. Experimental

All devices studied in this work were fabricated in a 1×20 crossbar array on SiO_2 (150 nm)/Si substrates, as illustrated in Fig. 1a. Both the bottom and top electrodes were patterned by photo lithography, and subsequently 30 nm thick Pt film with

5 nm thick Ti adhesion layer was deposited by e-beam evaporation and adopted as the electrodes after lift-off processes. Each cell has a size of 2×2 μm², as shown in the scanning electron microscopy (SEM) image in Fig. 1b. We have prepared four different transition metal oxide based bilayer structures varied in stacking sequence and material/composition, namely TaO_y/Ta_2O_{5-x}, Ta_2O_{5-x}/TaO_y, WO_z-50%/TaO_y and Ta_2O_{5-x}/WO_z-10%, as the switching materials of the devices, in which the oxygen-rich Ta_2O_{5-x} and WO_z-50% layers largely decide the overall device resistance and thus serve as the switching layers while the oxygen-deficient TaO_y and WO_z-10% films act as the base layers. The thicknesses of the switching layer and the base
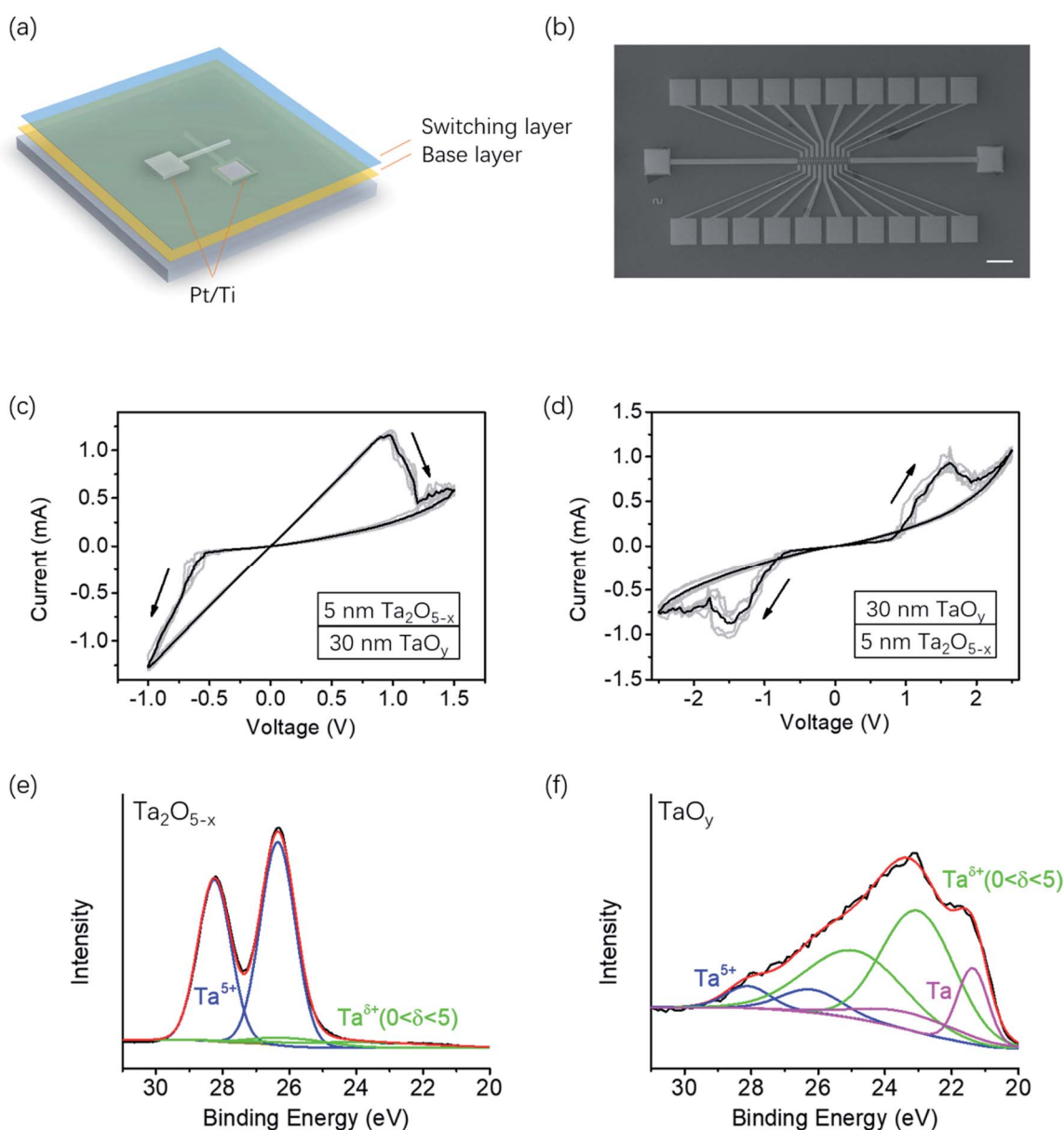

Fig. 1 (a) Schematic of the bilayer device structure. (b) SEM image of the 1×20 crossbar array. Scale bar: 100 μm. (c) 5 consecutive I−V sweeps (gray) and averaged I−V curve (black) of a Pt/Ti/Ta_2O_{5-x}/TaOy/Pt device. (d) 5 consecutive I−V sweeps (gray) and averaged I−V curve (black) of a Pt/Ti/Ta_2O_{5-x}/TaO_y/Pt device. (d) 5 consecutive I−V sweeps (gray) and averaged I−V curve (black) of a Pt/Ti/TaO_y/Ta_2O_{5-x}/Pt device. (e, f) Ta 4f XPS spectra obtained from the blank Ta_2O_{5-x} and TaO_y film, respectively. Blue, green and magenta lines correspond to Ta 4f doublets from the fully oxidic, suboxidic and metallic states, respectively.

layer were always fixed to ∼30 nm and ∼5 nm, respectively. The Ta_2O_{5-x} layer was prepared by radio frequency (RF) sputtering of a nominally stoichiometric Ta_2O_5 target, while the TaO_y layer was deposited by direct current (DC) reactive sputtering of a Ta metal target in Ar/O_2 gas mixture (the oxygen partial pressure was 3%) at 400 °C (more details can be found in our previous work[40]). The WO_z-50% and WO_z-10% films with different oxygen concentrations were deposited by reactive sputtering in Ar/O_2 gas mixture using a W metal target, and the percentage following WO_z denotes the oxygen partial pressure that was experimentally used in depositions. Electrical measurements including DC and pulse tests were performed using an Agilent B1500A semiconductor parameter analyzer together with a probe station. The electrical stimuli were always applied on the top electrodes with bottom electrodes grounded. The microstructure of the devices was analysed by high-resolution transmission electron microscopy (HRTEM) and scanning transmission electron microscopy (STEM). The compositions and chemical states of the oxides were analyzed by X-ray photoelectron spectroscopy (XPS), together with detailed peak deconvolutions. The values of x and y in Ta_2O_{5-x} and TaO_y have been extracted by XPS, which were found to be ∼0.4 and ∼1.0, respectively.

3. Results and discussion

Fig. 1c and d show typical current–voltage (I–V) characteristics of $Pt/Ti/Ta_2O_{5-x}/TaO_y/Pt$ and $Pt/Ti/TaO_y/Ta_2O_{5-x}/Pt$ devices, respectively, where the stacking sequences of the Ta_2O_{5-x} and TaO_y films are opposite in these two structures. Despite the identical deposition conditions of Ta_2O_{5-x} and TaO_y films in both structures, the $Pt/Ti/Ta_2O_{5-x}/TaO_y/Pt$ and $Pt/Ti/TaO_y/Ta_2O_{5-x}/Pt$ devices exhibit distinct switching behaviors after electroforming. When the TaO_y film was sputtered before the Ta_2O_{5-x} film, the resultant $Pt/Ti/Ta_2O_{5-x}/TaO_y/Pt$ device shows typical bipolar switching (Fig. 1c), which can be well explained by the V_O exchange between the Ta_2O_{5-x} and TaO_y layers.[29,40,41] In this case, the more stoichiometric and thus more insulating Ta_2O_{5-x} layer on top serves as the switching layer where local filament formation/dissolution is deemed to take place, while the more oxygen-deficient and thus more conductive TaO_y layer beneath acts as the base layer and hence can be considered as a reservoir of oxygen vacancies (V_Os). The migration of oxygen vacancies from the oxygen-deficient TaO_y layer to the oxygen-rich Ta_2O_{5-x} layer and accompanying electrochemical redox reactions lead to a set process, while backward V_O migration and redox reactions result in a reset process.[29,40,41] Such difference in oxygen concentration in Ta_2O_{5-x} and TaO_y was clearly verified by detailed XPS analysis, as shown in Fig. 1e and f. The Ta 4f XPS spectrum of Ta_2O_{5-x} films (Fig. 1e) shows a dominant Ta 4f doublet with Ta $4f_{7/2}$ and $4f_{5/2}$ peaks located at 26.35 and 28.25 eV, respectively. These peaks are indicative of fully oxidized Ta^{5+} state, consistent with the property of RF sputtered films with roughly maintained stoichiometry with that of the target. In contrast, Fig. 1f shows the Ta 4f XPS spectrum of TaO_y films, where three distinct chemical states of Ta can be found after peak deconvolutions. Besides the Ta^{5+} doublet with the Ta

$4f_{7/2}$ peak located at 26.2 eV, a suboxidic and metallic Ta doublets can be clearly identified with Ta $4f_{7/2}$ peak shifted to 23 and 21.4 eV.[40] Such lowered valence state of Ta clearly demonstrates the oxygen-deficient nature of the TaO_y film and therefore verifies the role of TaO_y layer as the reservoir of oxygen vacancies in the bilayer. The gradient of oxygen concentration in the bilayer structure therefore defines the polarity of the bipolar switching in $Pt/Ti/Ta_2O_{5-x}/TaO_y/Pt$ devices, which is favorable for enhancing the stability of cyclic switching.[42,43] As a control experiment, we have also fabricated single-layer devices including $Pt/Ti/Ta_2O_{5-x}/Pt$ and $Pt/Ti/WO_z$-50%/Pt, which have shown generally increased switching voltages and low yields, as can been in ESI Fig. S1.†

When the TaO_y film was deposited after the Ta_2O_{5-x} film, however, the $Pt/Ti/TaO_y/Ta_2O_{5-x}/Pt$ device exhibits complementary resistive switching (CRS) behavior (Fig. 1d) that is distinct from that in Fig. 1c. CRS behavior was firstly put forward by combining two RS cells anti-serially stacked together with a common electrode.[44] In this case, one cell is always in OFF state at low voltages, leading to overall high resistance and thus high nonlinearity, while the device state is defined by the internal configuration of the two cells instead of the overall resistance. Such nonlinear behavior can be used to address the sneak current problem in passive crossbar memristor arrays,[42,44] and therefore will be desirable for reducing the power consumption of memristive neural networks. These different switching effects, in oxide bilayer where only the stacking sequence was reversed, can be ascribed to interfacial reactions between the electrode and oxides. When the TaO_y film was sputtered before Ta_2O_{5-x}, the Ta_2O_{5-x} film is in contact with the top electrode, where a 5 nm thick Ti adhesion layer exists between Ta_2O_{5-x} and Pt. Since Ti is a well-known oxygen getter material,[45] a portion of the Ta_2O_{5-x} film could be reduced and thus the effective thickness of the switching layer is expected to be smaller than the nominal deposition thickness of Ta_2O_{5-x}, i.e. 5 nm. On the contrary, when the TaO_y film was deposited after the Ta_2O_{5-x} film, the Ta_2O_{5-x} film is in immediate contact with the inert bottom Pt electrode where no Ti exists in between. As a consequence, the effective thickness of the switching layer will not be affected by the existence of Ti and thus is expected to be larger than that in $Pt/Ti/Ta_2O_{5-x}/TaO_y/Pt$ devices. Given the different effective Ta_2O_{5-x} thicknesses, it is possible for the V_Os to get depleted in the $Pt/Ti/TaO_y/Ta_2O_{5-x}/Pt$ structure, leading to the observed CRS behavior in Fig. 1d rather than the bipolar switching in $Pt/Ti/Ta_2O_{5-x}/TaO_y/Pt$ devices (Fig. 1c). This has been verified by the reappearance of bipolar switching when a Ti layer was inserted into the bottom interface of $Pt/Ti/TaO_y/Ta_2O_{5-x}/Pt$ devices (Fig. 2a) and also by detailed TEM characterization (Fig. 2b–e). Obviously, the Ta_2O_{5-x} film when in direct contact with Ti (Fig. 2d) is thinner than the Ta_2O_{5-x} without interfacial reactions with Ti (Fig. 2e), therefore clearly verifying our hypothesis that Ti has the effect of reducing a portion of Ta_2O_{5-x} film and the different resistance switching behaviors in Fig. 1c and d indeed originate from interfacial reactions. As a result, a subtle variation in the thickness of the switching layer is able to result in pronounced evolutions in switching characteristics, implying that the switching layer plays a dominant
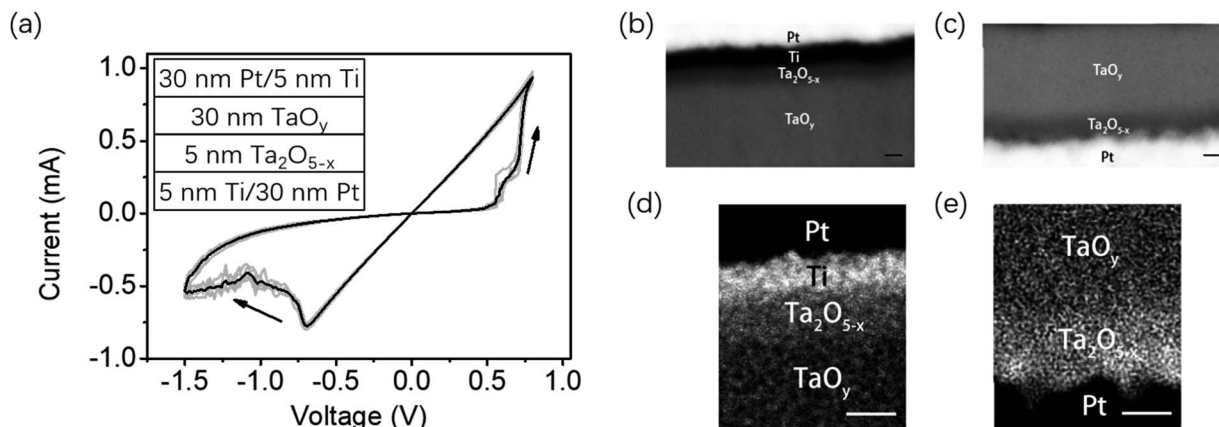
Fig. 2 (a) 5 consecutive $I-V$ sweeps (gray) and averaged $I-V$ curve (black) of a Pt/Ti/TaO$_y$/Ta$_2$O$_{5-x}$/Ti/Pt device. (b and c) Cross sectional STEM images of Pt/Ti/Ta$_2$O$_{5-x}$/TaO$_y$/Ti/Pt and Pt/Ti/TaO$_y$/Ta$_2$O$_{5-x}$/Pt devices. (d and e) Cross sectional HRTEM images of Pt/Ti/Ta$_2$O$_{5-x}$/TaO$_y$/Ti/Pt and Pt/Ti/TaO$_y$/Ta$_2$O$_{5-x}$/Pt devices. Scale bar: 5 nm.

role in resistive switching, which will be further discussed afterwards.

Furthermore, the conductance of memristors needs to be incrementally adjusted in order to serve as electronic synapses,[12,24,46,47] and we have thus studied the analog conductance modulation of the aforementioned memristive devices as well. Fig. 3a shows the pulse train used for measurements on Pt/Ti/Ta$_2$O$_{5-x}$/TaO$_y$/Pt devices, which contains a single, wide set pulse ($V_{\text{SET}} = -1.1$ V, $t_{\text{SET}} = 10$ ms) that ensures switching of the device to its highest conductance, followed by 50 narrower reset pulses with varied amplitudes ($V_{\text{RESET}} = 1.05-1.30$ V, $t_{\text{RESET}} = 200$ ns, $t_{\text{interval}} = 10$ ms) aiming to incrementally reduce the device conductance and cause synaptic depression. One can see that gradual conductance reductions can be obtained as the number of reset pulses increases (Fig. 3c), and the step of conductance change upon application of each pulse (ΔG) as well as the maximum adjustment range ($G_{\text{max}}/G_{\text{min}}$) can be facilely tailored by the amplitude of the applied pulses, as shown in Fig. 3c. In general, a higher V_{RESET} leads to larger ΔG and $G_{\text{max}}/G_{\text{min}}$ (Fig. 3c), and such controllability is desirable for implementing different learning rates in memristive neural networks. Similar conductance adjustments, *i.e.* ΔG and $G_{\text{max}}/G_{\text{min}}$ dependent on the amplitude of V_{SET} pulses, can also be achieved in potentiation processes, as shown in Fig. 3b and d. However, the conductance adjustment in potentiation (Fig. 3d) seems more abrupt compared with that in depression (Fig. 3c). This can be explained by the fact that the V$_{\text{O}}$ drift driven by the applied electric field and the V$_{\text{O}}$ diffusion caused by the V$_{\text{O}}$ concentration gradient in the bilayer films are in the same direction during potentiation, *i.e.* both flowing from TaO$_y$ to Ta$_2$O$_{5-x}$, so that the V$_{\text{O}}$ movement is accelerated (Fig. 3d). In stark contrast, the V$_{\text{O}}$ drift and diffusion are in opposite directions in depression, where reversed electric field is applied but the V$_{\text{O}}$ concentration gradient remains the same, therefore resulting in the overall more gradual conductance modulation observed in Fig. 3c.

Fig. 3e–h further shows the conductance evolution of Pt/Ti/TaO$_y$/Ta$_2$O$_{5-x}$/Pt devices when programming pulses with various amplitudes and polarities were applied. Similar with the Pt/Ti/Ta$_2$O$_{5-x}$/TaO$_y$/Pt devices, the ΔG and $G_{\text{max}}/G_{\text{min}}$ are also strongly dependent on the amplitudes of the applied potentiation and depression pulses. Nevertheless, it can be clearly observed that the device conductance in Pt/Ti/TaO$_y$/Ta$_2$O$_{5-x}$/Pt goes through a 2-regime evolution process when the pulse amplitude exceeds -2.3 V (Fig. 3e and g) or 1.6 V (Fig. 3f and h), where the device conductance increases first and then decreases. Such behavior is consistent with the CRS effect in Pt/Ti/TaO$_y$/Ta$_2$O$_{5-x}$/Pt devices as observed in DC measurements and once again indicates the influence of the switching layer thickness (Fig. 1c).[48]

Based on the above analysis, it is obvious that the base layer and the switching layer in an oxide bilayer structure play different roles in filament growth/dissolution and resistive switching dynamics. In general, the base layer serves as a reservoir of oxygen vacancies, while the filament formation/dissolution mainly takes place in the switching layer. This therefore indicates that the optimization of synaptic plasticity, *e.g.* the NOS, should be mainly performed on the material properties and defect structures of the switching layer. Tantalum oxide is a well-recognized material system with few thermodynamically stable intermediate oxide phases.[43,49] As a result, the analog conductance state of the devices should mainly originate from the geometry of the conduction channels, including the length and width of the filaments.[14] This to certain extent limits the NOS in tantalum oxide based memristive synapses. It is therefore of interest to replace tantalum oxide with other materials with rich intermediate phases and investigate the analog switching properties.

In light of this, we have introduced tungsten oxide as the new switching layer, which has been reported to have a large number of intermediate oxide phases including magneli phases.[50] Fig. 4a shows the schematic of the Pt/Ti/WO$_z$-50%/TaO$_y$/Pt devices, where the WO$_z$-50% layer deposited using a high oxygen partial pressure of 50% in reactive sputtering was used to replace Ta$_2$O$_{5-x}$ and served as the switching layer while the base layer was still TaO$_y$. The W 4f XPS spectrum of the
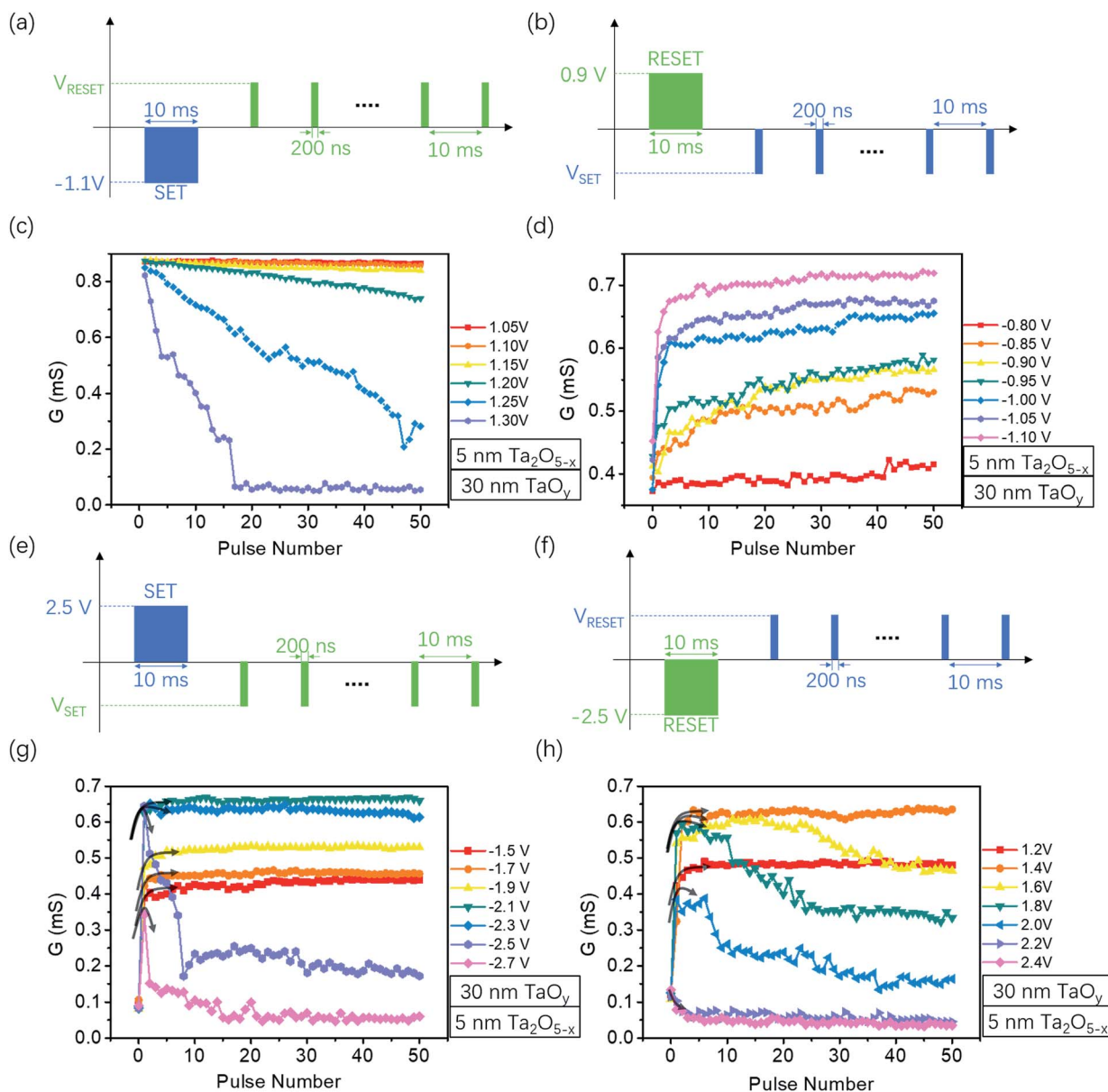
Fig. 3 (a, b) Schematic of pulse trains used for the long-term depression (LTD) and long-term potentiation (LTP) measurements with the Pt/Ti/Ta$_2$O$_{5-x}$/TaO$_y$/Pt device. (c, d) LTD and LTP of the Pt/Ti/Ta$_2$O$_{5-x}$/TaO$_y$/Pt. (e, f) Schematic of pulse trains used for LTD and LTP measurements with the Pt/Ti/TaO$_y$/Ta$_2$O$_{5-x}$/Pt device. (g, h) LTD and LTP of the Pt/Ti/TaO$_y$/Ta$_2$O$_{5-x}$/Pt devices.

WO$_z$-50% film (Fig. 4c) shows a dominant W 4f doublet with W 4f$_{7/2}$ and 4f$_{5/2}$ peaks located at 36 and 38.15 eV, respectively, suggesting that the WO$_z$-50% film is nearly fully oxidized and can indeed serve as the switching layer of the device. As expected, the Pt/Ti/WO$_z$-50%/TaO$_y$/Pt devices exhibit typical bipolar switching, as shown in Fig. 4b, and the switching polarity is consistent with the built-in gradient of oxygen concentration in the WO$_z$-50%/TaO$_y$ bilayer. Fig. 3d–g further show the potentiation and depression processes in Pt/Ti/WO$_z$-50%/TaO$_y$/Pt devices based on pulse measurements. Compared with the conductance adjustments in Pt/Ti/Ta$_2$O$_{5-x}$/TaO$_y$/Pt devices where Ta$_2$O$_{5-x}$ serves as the switching layer (Fig. 3c and d), it is obvious that the Pt/Ti/WO$_z$-50%/TaO$_y$/Pt devices with

WO$_z$-50% as the switching layer have shown larger NOS and better analog switching characteristics (Fig. 4f and g). A direct comparison of the pulse measurement results in different systems is shown in ESI Fig. S2.† The conductance of the Pt/Ti/WO$_z$-50%/TaO$_y$/Pt devices can also be changed in a more gradual manner in both potentiation and depression processes. The ΔG and G_{max}/G_{min} are once again dependent on the amplitudes of the potentiation and depression pulses.

The observed increase of NOS in Pt/Ti/WO$_z$-50%/TaO$_y$/Pt devices is expected to originate from the existence of rich intermediate oxide phases in tungsten oxide, as proposed above. Therefore, besides the geometric changes in conducting filaments upon application of potentiation and depression
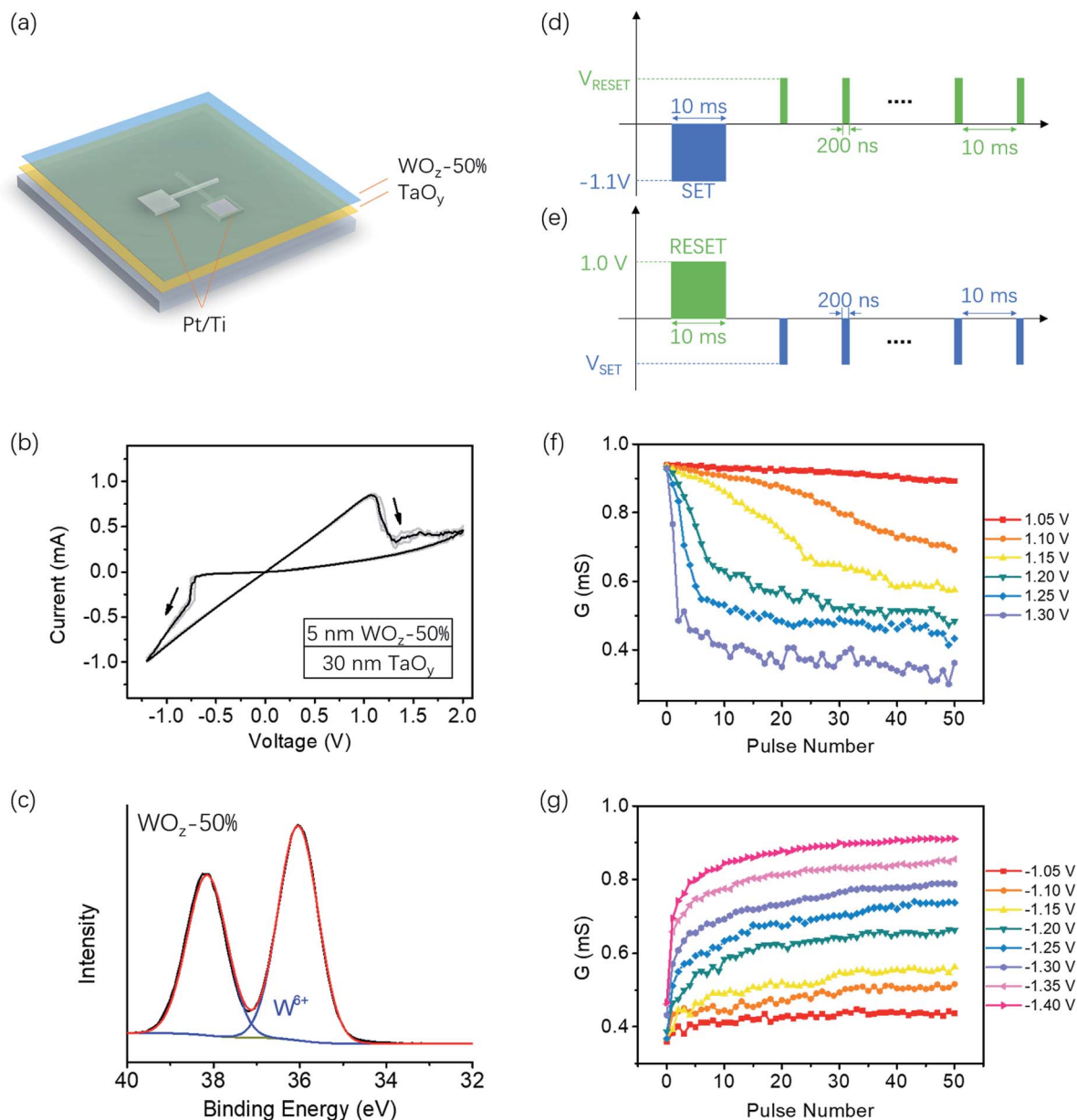
Fig. 4 (a) Schematic of the Pt/Ti/WO$_z$-50%/TaO$_y$/Pt device structure. (b) 5 consecutive $I-V$ sweeps (gray) and averaged $I-V$ curve (black) of a Pt/Ti/WO$_z$-50%/TaO$_y$/Pt device. (c) W 4f XPS spectra obtained from the blank WO$_z$-50% film. Blue lines correspond to W 4f doublets from the fully oxidic states. (d, e) Schematic of pulse trains used for LTD and LTP measurements with the Pt/Ti/WO$_z$-50%/TaO$_y$/Pt device. (f, g) LTD and LTP of the Pt/Ti/WO$_z$-50%/TaO$_y$/Pt device.

pulses, it is possible for some localized parts of the conduction channel to undergo phase transitions between the intermediate oxide phases of WO$_z$, further contributing to the incremental switching and thus the NOS. The applied electric field on the devices and the relatively strong thermal effects during device operations (with electrical conductance at ~mS level) can provide sufficient driving force for such localized phase transitions. An example of such phase transitions in WO$_z$ between the mother phase and a magnéli phase has been experimentally verified by transmission electron microscopy observations[24] and found responsible for the resistive switching in this system. It is worthwhile noting that in the case of analog switching the

conducting filament does not have to undergo phase transitions as a whole. Instead, only localized phase transitions in parts of the conduction channel will suffice in adjusting the device conductance in an incremental way, leading to the fine analog switching observed in Fig. 4f and g when the phase transition processes are coupled with the geometric changes of conducting filaments.

In order to verify this hypothesis, we have also fabricated control devices where tungsten oxide was used as the base layer instead of the switching layer (Fig. 5a). The oxygen partial pressure was reduced to 10% during the deposition of WO$_z$ in order to increase the concentration of oxygen vacancies,
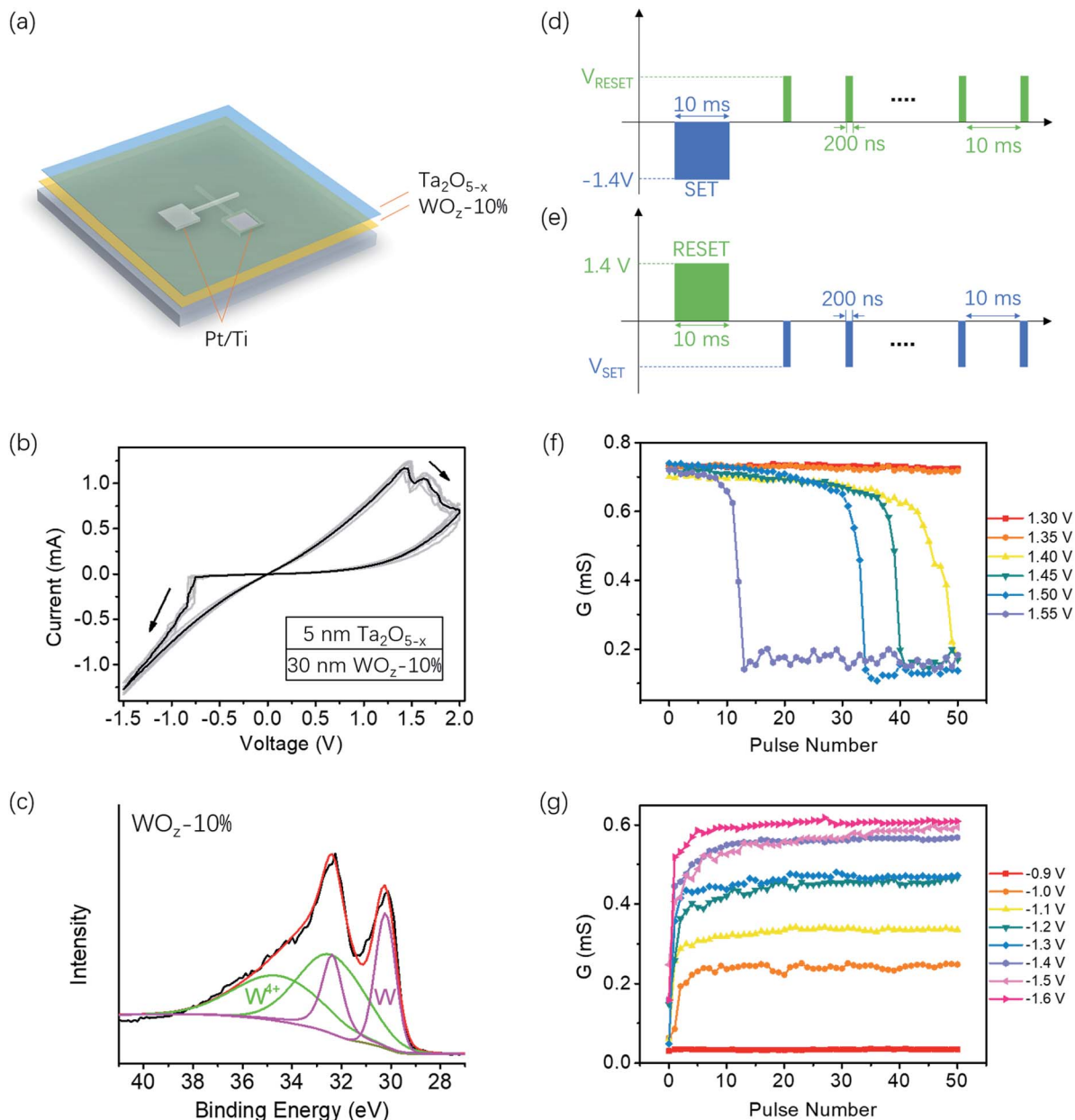
Fig. 5 (a) Schematic of the Pt/Ta$_2$O$_{5-x}$/WO$_z$-10%/Pt device structure. (b) 5 consecutive I–V sweeps (gray) and averaged I–V curve (black) of a Pt/Ti/Ta$_2$O$_{5-x}$/WO$_z$-10%/Pt device. (c) W 4f XPS spectra obtained from the blank WO$_z$-10% film. Green and magenta lines correspond to W 4f doublets from the suboxidic and metallic states, respectively. (d, e) Schematic of pulse trains used for LTD and LTP measurements with the Pt/Ti/Ta$_2$O$_{5-x}$/WO$_z$-10%/Pt device. (f, g) LTD and LTP of the Pt/Ti/Ta$_2$O$_{5-x}$/WO$_z$-10%/Pt.

therefore forming a Pt/Ti/Ta$_2$O$_{5-x}$/WO$_z$-10%/Pt structure. The XPS spectrum from the WO$_z$-10% film clearly shows existence of reduced W and metallic W states in the film (green and magenta doublets) and hence increased V$_O$ concentration in the film, as shown in Fig. 5c. A typical oxide bilayer is thus formed when the more oxygen-deficient WO$_z$ film is stacked with oxygen-rich Ta$_2$O$_{5-x}$, and the devices once again display typical bipolar switching characteristics (Fig. 5b). However, since the WO$_z$ was used as the base layer instead of the switching layer in the present Pt/Ti/Ta$_2$O$_{5-x}$/WO$_z$-10%/Pt structure, the switching characteristics are now mainly decided by Ta$_2$O$_{5-x}$ and thus the

intermediate states in WO$_z$ do not effectively contribute to the analog switching, unlike in Pt/Ti/WO$_z$-50%/TaO$_y$/Pt devices. As a result, the switching of the Pt/Ti/Ta$_2$O$_{5-x}$/WO$_z$-10%/Pt devices becomes very abrupt and the NOS largely decreases, as shown in Fig. 5d–g, which strongly demonstrates that the incremental switching behavior and the NOS are indeed correlated with the number of intermediate oxide phases in the switching layer.

We have further examined the above hypothesis in other transition metal oxide systems, and Fig. 6a summarizes the reported NOS values in memristive synapses based on four different transition metal oxides that have been reported
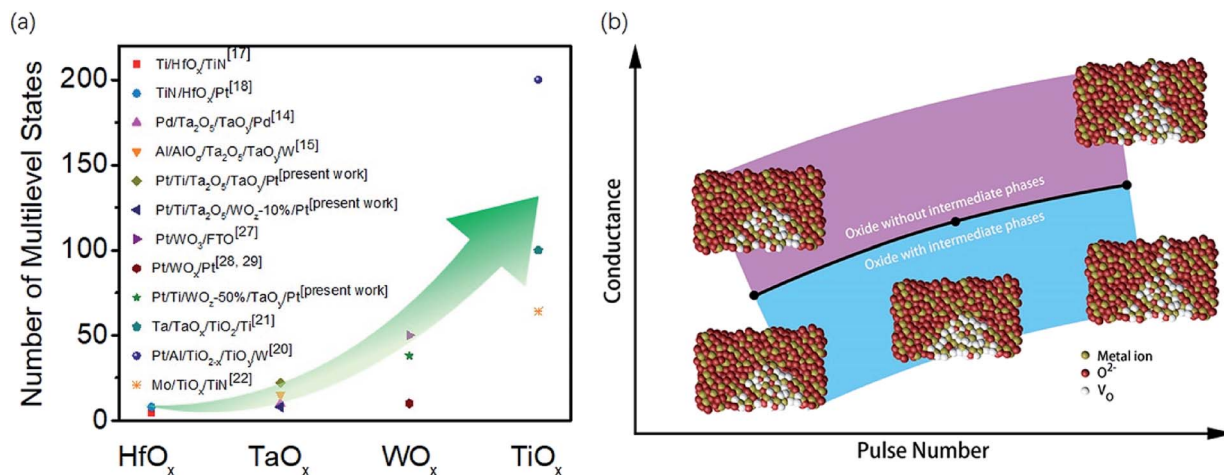
Fig. 6 (a) The number of multilevel states in four transition metal oxides based memristive synapses. (b) Schematic of the conductance change mechanism in oxide systems with and without intermediate phases, leading to different NOS.

previously,[14,15,17,18,20–22,27–29] where HfO_x and TaO_x are typical material systems with few thermodynamically stable oxide phases while WO_x and TiO_x represent material systems with rich intermediate phases.[40,43,49–52] The extraction of NOS should takes into account the noise level and conductance change that could be recognized (ESI Table S1 and related discussions†). It is obvious in Fig. 6a that WO_x and TiO_x based synaptic devices have generally shown much higher NOS compared with HfO_x and TaO_x, once again verifying that there is indeed an underlying correlation between the NOS and the number of phases in oxide memristors. This correlation is schematically depicted in Fig. 6b, where the existence of intermediate phases provides more conductance levels when coupled with the geometric changes of filaments, compared with oxides with few thermodynamically stable intermediate phases.

We would like to finally note that here we have concentrated on tailoring the number of conductance states, which is an important criterion for memristive synapses, but other characteristics of the cells such as endurance, retention *etc.* will put additional constraints on the synaptic devices and sometimes have different requirements on material properties. It is also likely to have some extent of intermixing between the switching layer and the base layer, due to inevitable inter-diffusion, as verified by XPS depth profiling analysis (ESI Fig. S3†). The present findings, however, could provide important clues to the optimization of memristive cells for future neuromorphic computing applications.

4. Conclusions

In summary, we have systematically studied the influence of materials, compositions and stacking sequences of oxide bilayer on the analog switching characteristics of memristive synapses. The results unambiguously showed the dominant role of the switching layer in deciding the analog switching properties and therefore device optimizations should be concentrated on the switching layer. Furthermore, compared with oxides with few

thermodynamically stable intermediate phases, it was found that the existence of rich intermediate phases could lead to larger NOS and thus more gradual resistive switching. These findings could be important for future device optimizations and constructions of neuromorphic computing systems.

Conflicts of interest

There are no conflicts of interest to declare.

Acknowledgements

References

1 L. O. Chua, *IEEE Trans. Circuit Theory*, 1971, **18**, 507–519.
2 D. B. Strukov, G. S. Snider, D. R. Stewart and R. S. Williams, *Nature*, 2008, **453**, 80–83.
3 J. J. Yang, D. B. Strukov and D. R. Stewart, *Nat. Nanotechnol.*, 2013, **8**, 13–24.
4 R. Waser, R. Dittmann, G. Staikov and K. Szot, *Adv. Mater.*, 2009, **21**, 2632–2663.
5 R. Waser and M. Aono, *Nat. Mater.*, 2007, **6**, 833–840.
6 Y. Yang, P. Gao, S. Gaba, T. Chang, X. Pan and W. Lu, *Nat. Commun.*, 2012, **3**, 732.
7 Y. Yang, P. Gao, L. Li, X. Pan, S. Tappertzhofen, S. Choi, R. Waser, I. Valov and W. D. Lu, *Nat. Commun.*, 2014, **5**, 4232.
8 N. K. Upadhyay, S. Joshi and J. J. Yang, *Sci. China. Inform. Sci.*, 2016, **59**, 061404.
9 M. Prezioso, F. Merrikh-Bayat, B. D. Hoskins, G. C. Adam, K. K. Likharev and D. B. Strukov, *Nature*, 2015, **521**, 61–64.

10 S. H. Jo, T. Chang, I. Ebong, B. B. Bhadviya, P. Mazumder and W. Lu, *Nano Lett.*, 2010, **10**, 1297–1301.

11 C. Du, W. Ma, T. Chang, P. Sheridan and W. D. Lu, *Adv. Funct. Mater.*, 2015, **25**, 4290–4299.

12 Y. Yang, B. Chen and W. D. Lu, *Adv. Mater.*, 2015, **27**, 7720–7727.

13 Y. Yang, M. Yin, Z. Yu, Z. Wang, T. Zhang, Y. Cai, W. D. Lu and R. Huang, *Adv. Electron. Mater.*, 2017, **3**, 1700032.

14 S. Kim, C. Du, P. Sheridan, W. Ma, S. Choi and W. D. Lu, *Nano Lett.*, 2015, **15**, 2203–2211.

15 X. Li, H. Wu, G. Bin, W. Wu, D. Wu, N. Deng, J. Cai and H. Qian, *Nanotechnology*, 2016, **27**, 305201.

16 B. Gao, Y. J. Bi, H. Y. Chen, R. Liu, P. Huang, B. Chen, L. F. Liu, X. Y. Liu, S. M. Yu, H. S. P. Wong and J. F. Kang, *ACS Nano*, 2014, **8**, 6998–7004.

17 Y.-E. Syu, T.-C. Chang, J.-H. Lou, T.-M. Tsai, K.-C. Chang, M.-J. Tsai, Y.-L. Wang, M. Liu and S. M. Sze, *Appl. Phys. Lett.*, 2013, **102**, 172903.

18 L. Zhao, H. Y. Chen, S. C. Wu, Z. Jiang, S. Yu, T. H. Hou, H. S. Wong and Y. Nishi, *Nanoscale*, 2014, **6**, 5698–5702.

19 A. Fabien, G. Ligang, D. H. Brian and B. S. Dmitri, *Nanotechnology*, 2012, **23**, 075201.

20 K. Seo, I. Kim, S. Jung, M. Jo, S. Park, J. Park, J. Shin, K. P. Biju, J. Kong, K. Lee, B. Lee and H. Hwang, *Nanotechnology*, 2011, **22**, 254023.

21 L. Gao, I. T. Wang, P. Y. Chen, S. Vrudhula, J. S. Seo, Y. Cao, T. H. Hou and S. Yu, *Nanotechnology*, 2015, **26**, 455204.

22 J. Park, M. Kwak, K. Moon, J. Woo, D. Lee and H. Hwang, *IEEE Electron Device Lett.*, 2016, **37**, 1559–1562.

23 T. Chang, S.-H. Jo and W. Lu, *ACS Nano*, 2011, **5**, 7669–7676.

24 Z. H. Tan, R. Yang, K. Terabe, X. B. Yin, X. D. Zhang and X. Guo, *Adv. Mater.*, 2016, **28**, 377–384.

25 R. Yang, K. Terabe, G. Liu, T. Tsuruoka, T. Hasegawa, J. K. Gimzewski and M. Aono, *ACS Nano*, 2012, **6**, 9515–9521.

26 T. Shi, X. B. Yin, R. Yang and X. Guo, *Phys. Chem. Chem. Phys.*, 2016, **18**, 9338–9343.

27 D. Kuzum, S. Yu and H. S. Wong, *Nanotechnology*, 2013, **24**, 382001.

28 R. Yang, K. Terabe, Y. P. Yao, T. Tsuruoka, T. Hasegawa, J. K. Gimzewski and M. Aono, *Nanotechnology*, 2013, **24**, 384003.

29 M.-J. Lee, C. B. Lee, D. Lee, S. R. Lee, M. Chang, J. H. Hur, Y.-B. Kim, C.-J. Kim, D. H. Seo, S. Seo, U. I. Chung, I.-K. Yoo and K. Kim, *Nat. Mater.*, 2011, **10**, 625–630.

30 S. H. Chang, S. B. Lee, D. Y. Jeon, S. J. Park, G. T. Kim, S. M. Yang, S. C. Chae, H. K. Yoo, B. S. Kang, M. J. Lee and T. W. Noh, *Adv. Mater.*, 2011, **23**, 4063–4067.

31 X. Liu, S. M. Sadaf, M. Son, J. Shin, J. Park, J. Lee, S. Park and H. Hwang, *Nanotechnology*, 2011, **22**, 475702.

32 J. Lee, C. Du, K. Sun, E. Kioupakis and W. D. Lu, *ACS Nano*, 2016, **10**, 3571–3579.

33 J. J. Yang, J. Borghetti, D. Murphy, D. R. Stewart and R. S. Williams, *Adv. Mater.*, 2009, **21**, 3754–3758.

34 M.-K. Kim and J.-S. Lee, *ACS Appl. Mater. Interfaces*, 2016, **8**, 32918–32924.

35 S.-M. Lin, J.-Y. Tseng, T.-Y. Su, Y.-C. Shih, J.-S. Huang, C.-H. Huang, S.-J. Lin and Y.-L. Chueh, *ACS Appl. Mater. Interfaces*, 2014, **6**, 17686–17693.

36 P. Bousoulas, P. Asenov, I. Karageorgiou, D. Sakellaropoulos, S. Stathopoulos and D. Tsoukalas, *J. Appl. Phys.*, 2016, **120**, 154501.

37 R. Huang, X. Yan, K. A. Morgan, M. D. B. Charlton and C. H. de Groot, *J. Phys. D: Appl. Phys.*, 2017, **50**, 175101.

38 G. Niu, M. A. Schubert, S. U. Sharath, P. Zaumseil, S. Vogel, C. Wenger, E. Hildebrandt, S. Bhupathi, E. Perez, L. Alff, M. Lehmann, T. Schroeder and T. Niermann, *Nanotechnology*, 2017, **28**, 215702.

39 K. Park and J.-S. Lee, *RSC Adv.*, 2016, **6**, 21736–21741.

40 Y. C. Yang, S. Choi and W. Lu, *Nano Lett.*, 2013, **13**, 2908–2915.

41 Y. C. Yang, J. Lee, S. Lee, C. H. Liu, Z. H. Zhong and W. Lu, *Adv. Mater.*, 2014, **26**, 3693–3699.

42 Y. C. Yang, P. Sheridan and W. Lu, *Appl. Phys. Lett.*, 2012, **100**, 203112.

43 J. J. Yang, M. X. Zhang, J. P. Strachan, F. Miao, M. D. Pickett, R. D. Kelley, G. Medeiros-Ribeiro and R. S. Williams, *Appl. Phys. Lett.*, 2010, **97**, 232102.

44 E. Linn, R. Rosezin, C. Kugeler and R. Waser, *Nat. Mater.*, 2010, **9**, 403–406.

45 J. J. Yang, J. P. Strachan, F. Miao, M. X. Zhang, M. D. Pickett, W. Yi, D. A. A. Ohlberg, G. Medeiros-Ribeiro and R. S. Williams, *Appl. Phys. A: Mater. Sci. Process.*, 2011, **102**, 785–789.

46 Z. Wang, S. Joshi, S. E. Savel'ev, H. Jiang, R. Midya, P. Lin, M. Hu, N. Ge, J. P. Strachan, Z. Li, Q. Wu, M. Barnell, G. L. Li, H. L. Xin, R. S. Williams, Q. Xia and J. J. Yang, *Nat. Mater.*, 2017, **16**, 101–108.

47 T. Ohno, T. Hasegawa, T. Tsuruoka, K. Terabe, J. K. Gimzewski and M. Aono, *Nat. Mater.*, 2011, **10**, 591–595.

48 X. Zhu, C. Du, Y. Jeong and W. D. Lu, *Nanoscale*, 2017, **9**, 45–51.

49 S. P. Garg, N. Krishnamurthy, A. Awasthi and M. Venkatraman, *J. Phase Equilib.*, 1997, **18**, 407.

50 M. Katoh and Y. Takeda, *Jpn. J. Appl. Phys., Part 1*, 2004, **43**, 7292–7295.

51 H. Okamoto, *J. Phase Equilib. Diffus.*, 2008, **29**, 124.

52 P. G. Wahlbeck and P. W. Gilles, *J. Am. Ceram. Soc.*, 1966, **49**, 180–183.